JGR Planets

RESEARCH ARTICLE
10.1029/2022JE007456

CO_2 Ocean Bistability on Terrestrial Exoplanets

R. J. Graham[1], Tim Lichtenberg[1], and Raymond T. Pierrehumbert[1]

[1]Atmospheric, Oceanic and Planetary Physics, Department of Physics, University of Oxford, Oxford, UK

Key Points:

- At low instellations within the circumstellar habitable zone, rocky planets with H_2O oceans may also develop oceans of condensed CO_2
- CO_2-ocean-bearing climate states are bistable with more traditional Earth-like climates where only water condenses at the planetary surface
- CO_2 oceans may occur even in the presence of the negative feedback on planetary climate provided by silicate weathering

Correspondence to:

R. J. Graham,
robert.graham@physics.ox.ac.uk

Citation:

Graham, R. J., Lichtenberg, T., & Pierrehumbert, R. T. (2022). CO_2 ocean bistability on terrestrial exoplanets. *Journal of Geophysical Research: Planets*, *127*, e2022JE007456. https://doi.org/10.1029/2022JE007456

Received 13 JUL 2022
Accepted 29 SEP 2022

Abstract Cycling of carbon dioxide between the atmosphere and interior of rocky planets can stabilize global climate and enable planetary surface temperatures above freezing over geologic time. However, variations in global carbon budget and unstable feedback cycles between planetary sub-systems may destabilize the climate of rocky exoplanets toward regimes unknown in the Solar System. Here, we perform clear-sky atmospheric radiative transfer and surface weathering simulations to probe the stability of climate equilibria for rocky, ocean-bearing exoplanets at instellations relevant for planetary systems in the outer regions of the circumstellar habitable zone. Our simulations suggest that planets orbiting G- and F-type stars (but not M-type stars) may display bistability between an Earth-like climate state with efficient carbon sequestration and an alternative stable climate equilibrium where CO_2 condenses at the surface and forms a blanket of either clathrate hydrate or liquid CO_2. At increasing instellation and with ineffective weathering, the latter state oscillates between cool, surface CO_2-condensing and hot, non-condensing climates. CO_2 bistable climates may emerge early in planetary history and remain stable for billions of years. The carbon dioxide-condensing climates follow an opposite trend in pCO_2 versus instellation compared to the weathering-stabilized planet population, suggesting the possibility of observational discrimination between these distinct climate categories.

Plain Language Summary On Earth, water is the only molecule that occurs in large quantities as both vapor and condensed phases, but that may not be the case for every planet. We simulate terrestrial exoplanets that receive less light from their stars than the Earth does. We find that CO_2 may build up to such high levels that it condenses out onto the planetary surface, allowing for oceans of liquid CO_2 and/or sheets of CO_2 clathrate to accumulate. Depending on factors like CO_2 outgassing rate, the kinds of silicate rocks present at the planetary surface, and the level of irradiation received by a given planet from its parent star, such oceans can remain stable for geologic-scale time periods, or a planet may oscillate back and forth between an Earth-like, non-CO_2-condensing state and an exotic CO_2-condensing state. Planets with liquid (or solid) CO_2 at their surface can have a profoundly different evolution than Earth, with important implications for their potential to host life.

1. Introduction

Earth's surface is dominated by a liquid water ocean in direct contact with the lithosphere. This state of affairs seems to be crucial for Earth's long-term climate stability and habitability, with the carbonate-silicate cycle modulating and stabilizing the planet's atmospheric CO_2 inventory through a set of water-rock chemical reactions taking place on the continents and seafloor (Berner et al., 1983; Coogan & Gillis, 2013; Penman et al., 2020; Walker et al., 1981). The carbonate-silicate cycle acts as a thermostat when CO_2 is a net greenhouse gas; however, when CO_2 builds to high enough levels, it increases planetary Rayleigh scattering and behaves as a coolant, which can convert the carbonate-silicate cycle into a destabilizing positive feedback. This suggests that otherwise Earth-like planets with large enough carbon inventories might be able to support climate configurations with high enough pCO_2 for either a hot, supercritical, Venus-like atmosphere at high instellations or an exotic, subcritical atmosphere with surface liquid CO_2 condensation coexisting with a liquid water ocean at low instellations. Planets of the latter variety might be difficult to remotely distinguish from more traditionally "Earth-like" planets lacking surface CO_2 condensation at equivalent orbits, but the geochemistry and potential habitability of these worlds would be radically different, even with a temperate surface climate. Most previous examinations of surface CO_2 condensation on terrestrial (exo)planets have focused on cold, glaciated climates where CO_2 would only condense as a solid (Bonati & Ramirez, 2021; Kadoya & Tajika, 2019; Turbet et al., 2017); waterworlds with high pressure ice mantles (Marounina & Rogers, 2020; Ramirez & Levi, 2018); or the potential for CO_2 condensation on Mars in the deep past (Forget et al., 2013; Kasting, 1991; Soto et al., 2015). In this study, we focus on surface CO_2 condensation on rocky exoplanets with temperate climates in different end-member weathering regimes that

inform the anticipated diversity of potentially habitable planets (Kasting et al., 1993; Wordsworth, Forget, Selsis, et al., 2010; von Paris et al., 2013).

From an astronomical perspective, carbon compounds are strongly depleted on the terrestrial planets of the Solar System relative to the nominal values in the Sun or the interstellar medium (Öberg & Bergin, 2021) as a result of processes operating in the protoplanetary disk (Krijt et al., 2020; Li et al., 2021) and on planetesimals (Hirschmann et al., 2021; Lichtenberg & Krijt, 2021). In addition, volatile partitioning into metal and melt phases can redistribute major carbon and hydrogen carriers between core, mantle, and atmospheric reservoirs and partly decouple the initially accreted volatile reservoir (Fischer et al., 2020; Grewal et al., 2020) from the atmospheric composition of rocky exoplanets. A recent example is provided by the outer TRAPPIST-1 planets, for which mass-radius contraints suggest volatile mass fractions on the order of several weight per cent (Agol et al., 2021). On a statistical level, the larger sub-Neptune cluster of the Kepler radius valley suggests that at least a fraction of systems accrete substantial volatile mass budgets during their formation (Venturini et al., 2020; Zeng et al., 2019). The anticipated variation in carbon abundance suggests that the majority of rocky exoplanets may exhibit diverse climate regimes, for which the thermodynamic limits to maintain clement surface states are poorly understood (Lichtenberg et al., 2022). Future exoplanet surveys that will aim to probe the atmospheres of temperate exoplanets to test the range of climate diversity (Checlair et al., 2021; Gaudi et al., 2020; Quanz, Absil, et al., 2021; Quanz, Ottiger, et al., 2021) will rely on physically motivated theories to interpret their findings.

Here, we study the interplay between silicate weathering and CO_2 pressure variations to probe the limits of clement climates on terrestrial exoplanets. We use 1-D, two-stream radiative transfer and carbon cycle simulations to investigate the behavior of climates with high partial pressure of CO_2 (pCO_2) and low irradiation from the central star (S_{eff}) without (Sections 3.1 and 3.2) and with (Section 3.3) weathering feedbacks. Our simulations suggest that terrestrial planets at low instellations in the classical circumstellar habitable zone (HZ; Kasting et al., 1993) may emerge from their accretionary period directly into stable climate states with long-lasting periods of liquid CO_2 surface condensation, even in cases where they are not initially globally glaciated.

2. Methods

In this study we combine global-mean, clear-sky climate and silicate weathering calculations to examine the interplay between radiative and geochemical feedbacks on ocean-bearing, high-pCO_2 planets in the outer reaches of the classical HZ. Here we briefly outline the procedure we follow and the models we use for the radiative calculations and the weathering calculations.

2.1. Radiative Transfer

We carry out radiative transfer calculations using the SOCRATES code (Edwards & Slingo, 1996), solving the plane-parallel, two-stream approximated radiative transfer equation with scattering (see the extensive description in Lichtenberg et al., 2021, though note that the implementation in that paper does not include scattering). Opacity coefficients are tabulated and derived from the HITRAN database, making use of the line-by-line and collision-induced absorption coefficients for H_2O (Gordon et al., 2017), CO_2 (Gordon et al., 2017; Gruszka & Borysow, 1997), N_2 (Gordon et al., 2017; Karman et al., 2015), and the H_2O continuum (Mlawer et al., 2012). We note that the CO_2 continuum spectrum is uncertain at high temperatures and pressures, which introduces a potentially significant source of error into our calculations (e.g., Halevy et al., 2009; Wordsworth, Forget, & Eymet, 2010).

Rayleigh scattering cross-sections for CO_2 and N_2 are calculated following Vardavas and Carver (1984).

$$\sigma_{R,i} = \frac{0.2756}{\mu_i} \times \frac{6+3\Delta}{\lambda^4(6-7\Delta)} \left[A \left(1 + \frac{B}{\lambda^2} \right) \right]^2, \quad (1)$$

where the subscript i iterates over the species present, $\sigma_{R,i}$ ($m^2\ kg^{-1}$) is the Rayleigh scattering cross-section, μ_i is the molar mass of species i (kg mol^{-1}), λ (μm) is wavelength, coefficients A and B are taken from Cox (2015), Δ is the depolarization factor, and the numerical values we use are given in Table 1. For H_2O, as far as we are aware, values for the coefficients A and B have not been published at the relevant wavelengths. For this reason,

Table 1
Tabulation of Rayleigh Scattering Data Used in This Study

Molecule	A (units of 10^{-6})	B (units of 10^{-3})	Δ	σ_0 (10^{-7} m^2 kg^{-1})
CO_2	4.39	6.4	0.0805	–
N_2	2.906	7.7	0.0305	–
H_2O	–	–	–	9.32

Note. A and B values come from Cox (2015). σ_0 for H_2O is drawn from Pierrehumbert (2010). Δ values come from Vardavas and Carver (1984).

and because H_2O is a minor constituent in the atmospheres we simulate, we use a simple λ^{-4} scaling to calculate H_2O's Rayleigh scattering cross-section,

$$\sigma_{R,H_2O} = \sigma_{R,0}\frac{\lambda_0^4}{\lambda^4}, \quad (2)$$

where $\sigma_{R,0} = 9.32 \times 10^{-7}$ m^2 kg^{-1} (Pierrehumbert, 2010) and $\lambda_0 = 1$ μm. Here we take the opportunity to note that some previous papers (Kopparapu et al., 2013; Pluriel et al., 2019), have erroneously used H_2O Rayleigh scattering coefficients calculated using a depolarization ratio that was drawn from a study (Marshall & Smith, 1990) of the scattering properties of *liquid* H_2O, not water vapor. The total Rayleigh scattering cross-section is calculated by summing the cross-sections of the individual species, weighted by volumetric mixing ratio,

$$\sigma_{R,\mathrm{tot}} = \sum_i x_i \sigma_{R,i}, \quad (3)$$

where x_i represents the volumetric mixing ratio of a given species ($\sum_i x_i = 1$). SOCRATES does not allow vertically-varying Rayleigh scattering coefficients, so we take the mixing ratios at the surface to calculate the total scattering cross-sections.

The primary stellar spectrum we use in the presented calculations is based on measurements of the Sun's spectral irradiance (Kurucz, 1995), and thus represents irradiation from a G2V star. To show how the climate behaviors we identify depend on stellar type and age, we also present sets of simulations using spectra from AD Leonis, an M3.5V star (Segura et al., 2005), and Sigma Boötis, an F2V star (Segura et al., 2003). The different spectra result in different planetary albedo values for a given atmospheric composition and climate. We also tested the effects of a change in the solar spectrum with time: at 4.5 and 3.8 Ga before present (Claire et al., 2012) our simulations produced results that differed negligibly from the fiducial, modern case.

We apply a generalized pseudoadiabat formula (Graham et al., 2021) to calculate atmospheric temperature-pressure profiles with a variety of compositions and surface boundary conditions. This pseudoadiabat formula incorporates the fraction of retained condensate as a freely tunable parameter which can significantly impact the specific heat capacity and lapse rate in atmospheres with non-dilute condensable species. In our calculations, we assume that all condensate is instantaneously rained out upon condensation. We also assume H_2O saturation in the main set of simulations discussed in this paper. This formula is useful because it allows us to self-consistently calculate atmospheric profiles with any combination of condensable (e.g., H_2O, CO_2) and non-condensable (e.g., N_2) gases, though the atmospheres we focus on in this paper are simply $CO_2 + H_2O$ (sensitivity tests with up to 10 bar of N_2 produced qualitatively identical results, as expected). Throughout this paper, unless otherwise noted, atmospheres are taken to have isothermal stratospheres with $T_{\mathrm{strat}} = 150$ K. This is comparable to the stratospheric temperatures hypothesized for high-CO_2 planets in the outer reaches of the classical circumstellar HZ (Kopparapu et al., 2013), and time-stepped radiative-convective calculations in high-pCO_2 atmospheres have recovered a stratospheric temperature of 150 K (Wordsworth & Pierrehumbert, 2013). Condensation of H_2O and CO_2 is assumed to cease within the stratosphere, so the mixing ratios remain constant at pressure levels below the highest pressure level (lowest altitude level) with a temperature of 150 K. Assuming a constant stratospheric temperature considerably simplifies our climate calculations (described further below), at the expense of neglecting the feedback between instellation and stratospheric temperature, which can change a planet's outgoing longwave radiation (OLR) and thus its surface temperature. Sensitivity tests carried out with an increased stratospheric temperature of up to 200 K demonstrate that the effect on climate is minor, with no qualitative changes to our results.

For rapid simulation of a wide range of surface conditions, we take an "inverse climate modeling" approach (Kasting, 1991). This entails choosing a pCO_2 and a surface temperature (which in turn specifies pH_2O by the Clausius-Clapeyron relation), using those values as boundary conditions to integrate the pseudoadiabat from the surface up to the 150 K isothermal stratosphere, and running the radiative transfer code to get the OLR and albedo for that specific atmospheric temperature/pressure/composition combination. With those values, we can calculate the instellation necessary to maintain global-mean energetic balance between incoming and outgoing radiation,

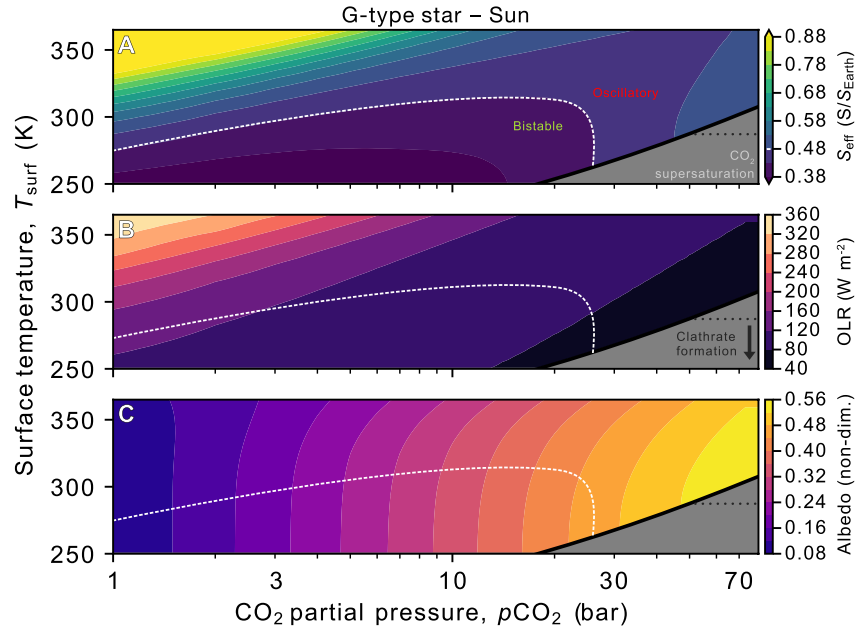

Figure 1. Energetic properties of terrestrial planetary climates at low instellation as a function of surface temperature T_{surf} (y-axes) and CO_2 partial pressure (x-axes). In each panel, the black line represents the CO_2 saturation vapor pressure curve; climates with CO_2 greater than that of the vapor pressure curve at a given temperature are super-saturated at their surface (gray region in all three panels). The white dotted line in each panel represents the approximate contour location of the S_{eff} value separating climates that can support CO_2 bistability versus those that may limit cycle between condensing and non-condensing states (see Sections 3.2 and 3.3 for discussion of those climate types). The black dotted line in each panel marks the temperature below which CO_2 clathrate hydrates may be stable. In panel A, the contours represent the top-of-atmosphere stellar irradiation required to maintain a climate with a given surface temperature and pCO_2, normalized by the instellation received at Earth's orbit, that is, $S/S_{Earth} = S_{eff}$. Panel (b) shows the global-mean outgoing longwave radiation. Panel (c) shows the global-mean planetary albedo.

$$(1 - \alpha(T, \mathrm{pCO_2}))\frac{S}{4} = F_{out}(T, \mathrm{pCO_2}), \tag{4}$$

$$S_{eff}\,(T, \mathrm{pCO_2}) = \frac{S}{S_{Earth}} = \frac{4F_{out}\,(T, \mathrm{pCO_2})}{S_{Earth}\,(1 - \alpha\,(T, \mathrm{pCO_2}))}, \tag{5}$$

where S is top-of-atmosphere instellation, $S_{Earth} = 1368$ W m^{-2} is Earth's present-day instellation, S_{eff} is the fraction of present-day Earth's instellation (e.g., $S_{eff} = 0.3$ is equivalent to 30% of present-day Earth instellation), F_{out} is the OLR, and α is the global-mean planetary albedo, with the cosine of the stellar zenith angle assumed to be the instellation-weighted global mean of $\frac{2}{3}$ in all calculations (Cronin, 2014). We also set the surface albedo to 0.0, similar to the albedo of a cloudless sea surface, which would be 2%–4% at the chosen stellar zenith angle (Li et al., 2006). Low-lying marine stratocumulus clouds that would increase the near-surface albedo to levels above that of the sea surface are expected to dissipate at CO_2 levels far lower than 1 bar, the lowest pCO_2 evaluated in this study, due to the inhibition of cloud-top radiative cooling and subsequent shutdown of cloud-sustaining lower-tropospheric convection (e.g., Schneider et al., 2019), though of course other processes could still cause low-lying clouds or hazes that would affect near-surface albedo on these planets.

We carried out a grid of these inverse climate calculations for pCO_2 levels ranging from 1 to 73 bar with increments of 1 bar and for T_{surf} from 250 to 365 K with increments of 5 K. Figure 1 shows equilibrium S_{eff} (panel a), OLR (panel b), and albedo (panel c), all as functions of T_{surf} and pCO_2. Linear interpolation of OLR and albedo to temperatures and pCO_2 levels between the climate grid points allows for fast climate calculations to examine a wide variety of scenarios.

Table 2
Model Parameters Used in This Study

Parameter	Units	Definition	Fiducial value
γ	–	Land fraction	0.3
a_g	–	Surface albedo	0.0
R_{planet}	meters (m)	Planetary radius	6.37×10^6
T_{ref}	Kelvin (K)	Reference global-avg. temperature	288
$pCO_{2,ref}$	bar	Reference CO_2 partial pressure	280×10^{-6}
q_{ref}	m yr^{-1}	Modern global-avg. runoff	0.20 (Oki et al., 2001)
ϵ	1/K	Fractional change in precip. per K change in temp.	0.03
V_{ref}	mol yr^{-1}	Modern global CO_2 outgassing	7.5×10^{12} (Gerlach, 2011; Haqq-Misra et al., 2016)
v	mol m^{-2} yr^{-1}	Modern CO_2 outgassing per m^2 planetary area	0.0147
Λ	Variable	Thermodynamic coefficient for C_{eq}	1.4×10^{-3}
n	–	Thermodynamic pCO_2 dependence	0.316
α*	–	$L\phi\rho_{sf}AX_r\mu$ (see Section 2.2 and below)	3.39×10^5
$k_{eff,ref}$*	mol m^{-2} yr^{-1}	Reference rate constant	8.7×10^{-6}
β	–	Kinetic weathering pCO_2 dependence	0.2 (Rimstidt et al., 2012)
T_e	Kelvin	Kinetic weathering temperature dependence	11.1 (Berner, 1994)

Note. This table lists parameters used in our calculations, their units, their definitions, and the default values they take. A single asterisk (*) means the default parameter value was drawn from Table S1 of the Supplement to Maher and Chamberlain (2014). For default parameters drawn from other sources, the citation is given in the "Value" column.

2.2. Carbon Cycling

To examine how the carbon cycle might operate on abiotic terrestrial planets under very high pCO_2 conditions, we apply an idealized global-mean weathering formulation (Graham & Pierrehumbert, 2020) based on work that accounts for the impact of clay precipitation on weathering solute concentrations (Maher & Chamberlain, 2014) on the global-mean weathering flux,

$$W = \gamma \frac{\alpha}{[k_{\text{eff}}]^{-1} + mAt_s + \alpha\left[qC_{\text{eq}}\right]^{-1}}, \tag{6}$$

where W (mol m^{-2} yr^{-1}) is the global-mean weathering flux, that is, the total number of divalent cations (which react with oceanic carbon to form carbonate minerals, ultimately removing CO_2 from the atmosphere) delivered to the ocean from the land and/or seafloor in a year, divided by the surface area of the planet; γ is the fraction of planetary surface that is weatherable; α is a parameter that captures the effects of various weathering zone properties like characteristic water flow length scale, porosity, ratio of mineral mass to fluid volume, and the mass fraction of minerals in the weathering zone that are weatherable; $k_{\text{eff}} = k_{\text{eff,ref}} \exp\left(\frac{T_{\text{surf}} - T_{\text{surf,ref}}}{T_e}\right)\left(\frac{pCO_2}{pCO_{2,\text{ref}}}\right)^{\beta}$ (mol m^{-2} yr^{-1}) is the effective kinetic weathering rate, that is, the weathering rate in the absence of chemical equilibration with clay precipitation (Walker et al., 1981); m (kg mol^{-1}) is the average molar mass of minerals being weathered; A (m^2 kg^{-1}) is the average specific surface area of the minerals being weathered; t_s (yr) is the mean age of the material being weathered; $q = q_{\text{ref}}(1 + \epsilon(T_{\text{surf}} - T_{\text{surf,ref}}))$ (m yr^{-1}) is the volume-weighted global-mean flux of water through the planet's weathering zones (in this study we apply a linear temperature dependence to runoff, based on the behavior of surface H_2O precipitation on Earth, but we note that the functional form for q could be very different when modeling seafloor weathering); and $C_{\text{eq}} = \Lambda\left(pCO_2\right)^n$ (mol m^{-3}) is the maximum concentration of divalent cations in the water passing through weathering zones, as determined by chemical equilibrium between silicate dissolution and clay precipitation. The values of all constants are given in Table 2. A more thorough set of weathering calculations would carefully account for the lithology of minerals being weathered (Hakim et al., 2021) and the differences between continental and seafloor weathering (Hakim et al., 2021; Hayworth & Foley, 2020), but our calculations are meant to be illustrative of the qualitative behavior

of the carbon cycle under non-terrestrial conditions, so we restrict our simulations to the simplified approach in our Equation 6.

Assuming the presence of weatherable silicates on a planetary surface, the global weathering flux of divalent cations into the ocean, which is equal to the global CO_2 consumption flux at equilibrium and in the absence of CO_2 surface condensation, is dependent on both background CO_2 and T_{surf}. An increase to pCO_2 or T_{surf} leads to an increase in the weathering rate, with the change mediated by either changes to the kinetics of silicate dissolution or changes to global runoff flux, depending on which term in Equation 6 is dominant. This climate-dependence of CO_2 consumption means that silicate weathering can act as a stabilizing negative feedback on planetary climate (Walker et al., 1981). If the CO_2 outgassing flux from volcanoes and other sources (V) is greater than the CO_2 consumption flux from weathering, that is, if $V > W$, and if there is no CO_2 surface condensation, CO_2 will accumulate in the atmosphere, which, under Earth-like circumstances, tends to warm the planet. Higher pCO_2 and higher T_{surf} both lead to larger W, driving the CO_2 consumption rate closer and closer to V until CO_2 consumption is equal to CO_2 production and the atmospheric CO_2 inventory stabilizes. The same process in reverse acts to cool the planet and equilibrate the carbon cycle in cases where $W > V$. So, at least in the cases just discussed, climate on planets with silicate weathering will tend to find an equilibrium T_{surf} and pCO_2 determined by the balance between silicate weathering and CO_2 outgassing, which can be stated simply as

$$V = W, \tag{7}$$

where V (mol m^{-2} yr^{-1}) is an assumed CO_2 outgassing flux and W is the weathering flux as defined in Equation 6. The intersection points in T_{surf}–pCO_2 space of the nullclines given by Equations 4 and 7 are climate states in equilibrium with respect to both energy and carbon fluxes.

The weathering parameterization represented by Equations 6 and 7 implies the assumption of an Earth-like tectonic regime where the resurfacing of fresh silicates occurs rapidly enough to maintain a weathering flux in balance with CO_2 outgassing. This need not be the case: for example, if a planet is in a "sluggish lid", "episodic lid", or "stagnant lid" tectonic regime (e.g., Foley, 2015; Kite et al., 2009; Korenaga, 2010; Lenardic, 2018; Lichtenberg et al., 2022; Valencia & O'Connell, 2007), resurfacing may not be fast enough for weathering to keep up with the outgassing rate, leading to a global depletion of weatherable materials called "supply limitation" (West et al., 2005) or "transport limitation" (Kump et al., 2000), which in turn allows for volcanic CO_2 accumulation. Further, even with rapid tectonic resurfacing, the particular climate and/or arrangement of land on a given planet may not allow for high enough weathering fluxes to match outgassing rates, as we will go on to demonstrate. For these cases, it is important to note that surface CO_2 condensation can act as another major sink of atmospheric CO_2 (Kasting, 1991; Wordsworth, Forget, Selsis, et al., 2010; von Paris et al., 2013; Turbet et al., 2017; Kadoya & Tajika, 2019; Bonati & Ramirez, 2021). As a result, under CO_2-condensing conditions, it is possible for the carbon cycle to reach equilibrium even when outgassing does not equal weathering, as condensation can make up the difference,

$$F_{cond} = V - W, \tag{8}$$

where F_{cond} (mol m^{-2} yr^{-1}) is the flux of CO_2 condensing out onto the surface from the atmosphere.

3. Results

3.1. Climate Hysteresis From Temperature-Dependent Instellation Absorption of H_2O

In climate simulations with high pCO_2, cooling by Rayleigh scattering begins to outweigh greenhouse warming, such that temperature eventually begins to decrease while CO_2 increases (Figure 1): in panel A, starting from the lowest $pCO_2 = 1$ bar, each contour of S_{eff} moves to higher temperatures as CO_2 increases, until a peak T_{surf} is reached at a threshold pCO_2, beyond which T_{surf} for a given S_{eff} begins to decrease as CO_2 increases. For instance, for $S_{eff} = 0.4$ this peak is at ≈280 K and $pCO_2 = 10$ bar. This occurs because, at high pCO_2, the albedo (panel C) increases more rapidly with pCO_2 than the OLR (panel B) decreases, since the atmosphere has become optically thick at almost all IR wavelengths. In other words, for any given S_{eff} and background gas composition, there is a maximum temperature that cannot be exceeded by adding CO_2 to the atmosphere. This effect has been used to define the outer edge of the classical liquid water HZ as the lowest instellation at which atmospheres with 1 bar N_2, saturated H_2O, and variable CO_2 can maintain an Earth-like planet's global-mean surface temperature

above freezing (Kasting et al., 1993; Kopparapu et al., 2013), that is, the S_{eff} where the peak temperature is $T_{surf} = 273.15$ K. Using this "maximum greenhouse limit," the outer edge of the liquid water HZ has been placed at 1.67 astronomical units (au) (Kopparapu et al., 2013), implying $S_{eff} = \frac{1}{1.67^2} = 0.359$, with $pCO_2 \approx 6$–7 bar. Our fiducial simulations lack N_2, but, in comparison with Kopparapu et al. (2013), produce a similar value of $S_{eff} = 0.373$ for the lowest instellation where T_{surf} can be maintained above freezing, with $pCO_2 \approx 5$–6 bars, demonstrating our climate model produces comparable results to previous efforts.

At low values of S_{eff} (e.g., along the white-dotted $S_{eff} = 0.40$ contour in Figure 1a), we find that the climate responds smoothly to increases in pCO_2, with T_{surf} first increasing and then decreasing until reaching a pCO_2–T_{surf} combination that allows the CO_2 to condense at the surface. This is the point where a given S_{eff} contour intersects the black line that bounds the bottom-right gray area in Figure 1a. At this point CO_2 is saturated and our simulations assume that any CO_2 added to the atmosphere simply condenses out onto the surface.

As S_{eff} increases, the maximum temperature climates can reach becomes higher and higher. H_2O is saturated in our simulations and, as such, pH_2O increases exponentially with temperature. Therefore, as S_{eff} increases, water's impact on the climate also becomes more and more prominent. In addition to its well-known greenhouse effect, water can impact planetary albedo via several mechanisms, for instance via cloud and sea ice formation. Less obvious impacts of water on planetary albedo come from its contribution to Rayleigh scattering and its competing contribution to shortwave and near-IR absorption.

At low pCO_2 ($\lesssim$1.5 bar) and high temperatures where pH_2O is comparable to pCO_2, our simulations indicate that the Rayleigh scattering effect of water starts to become important, which is why the albedo contours bend leftward in the upper-left corner of Figure 1c, indicating an increase in albedo from enhanced H_2O Rayleigh scattering as temperature increases. However, at high enough CO_2 ($\gtrsim$1.5 bar), pCO_2 remains much larger than pH_2O even at the highest temperatures we simulated, and hence the Rayleigh scattering effect of H_2O is outweighed by that of CO_2. This suggests that increases to surface temperature up to 360 K stop significantly increasing a planet's Rayleigh scattering albedo via H_2O accumulation at pCO_2 above a few bar.

Although H_2O's Rayleigh scattering ceases to be important at high pCO_2, H_2O's shortwave and near-IR absorption remain important, such that the elevated water content caused by increased temperature leads to increased absorption of instellation: albedo and equilibrium S_{eff} decrease with increased temperature at high pCO_2, as indicated by the rightward tilt of S_{eff} and albedo contours in the upper-right quadrants of Figures 1a and 1c. In other words, at high pCO_2, H_2O saturation leads to temperature-dependent planetary albedo similar to that caused by the ice-albedo feedback, though occurring at temperatures higher than those where the ice-albedo feedback is relevant. This temperature-dependent instellation absorption by H_2O introduces a form of hysteresis into the climate system that is analogous to the hysteresis caused by the ice-albedo feedback (Abbot et al., 2018), the consequences of which we explore here.

3.2. CO_2 Ocean Oscillations on Temperate Exoplanets

Climate limit cycling usually refers to the potential for climates to oscillate back and forth between snowball and temperate states (Abbot, 2016; Haqq-Misra et al., 2016; Menou, 2015; Paradise & Menou, 2017). That occurs when a temperate planet on which weathering dominates outgassing has its CO_2 drawn down until the ice-albedo feedback triggers global glaciation. At this point weathering slows below the rate of outgassing and allows CO_2 to accumulate and eventual deglaciate the planet, which restarts the cycle. Our simulations indicate the existence of a distinct limit cycle that can emerge when outgassing dominates weathering: the oscillation between a CO_2 surface-condensing state and a non-CO_2-condensing state on planets with CO_2-H_2O atmospheres. This variety of limit cycling is a consequence of the temperature-dependent planetary albedo that arises from H_2O's shortwave and near-IR absorption, in combination with CO_2's Rayleigh scattering effect.

In Equation 4, energetic equilibrium between global-mean absorbed instellation and OLR is assumed, and each S_{eff} contour in Figure 1a is a set of T_{surf}–pCO_2 pairs where Equation 4 holds for that particular S_{eff} value. However, at high pCO_2, when S_{eff} is large enough to permit the high temperatures that raise water's vapor pressure enough to lower the planet's albedo substantially, the right-hand branches of the S_{eff} contours become energetically unstable to perturbations in temperature and pCO_2. The consequences of this phenomenon for planetary climate evolution are illustrated in Figure 2. In this figure, we plot the right-hand branch of the set of T_{surf} and pCO_2 values that produce energetic equilibrium with $S_{eff} = 0.46$. Any combination of T_{surf} and pCO_2 not falling on the dark red line

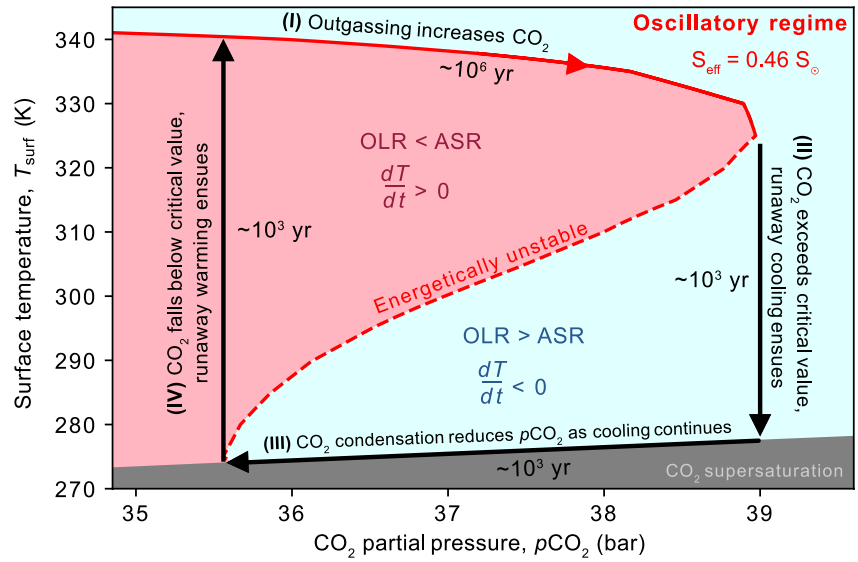

Figure 2. Climatic limit cycling driven by CO_2 outgassing, Rayleigh scattering, temperature-dependent near-IR stellar absorption by H_2O, and surface CO_2 condensation. In step (I), outgassing allows CO_2 to accumulate. In step (II), pCO_2 exceeds the value that triggers a positive feedback loop between cooling surface temperature and increasing planetary albedo. In step (III), the planetary surface temperature becomes low enough to trigger surface CO_2 condensation, so continued cooling now also decreases atmospheric pCO_2. In step (IV), a positive feedback loop between warming and albedo reduction from H_2O accumulation leads to runaway warming.

in Figure 2 leads to energetic disequilibrium under an instellation of $S_{eff} = 0.46$. This results in either cooling in the case where the planetary OLR is higher than the absorbed stellar radiation (OLR > ASR = $(1 - \alpha)S/4$) in the light blue region, or warming in the light red region, where ASR > OLR.

When the climate resides on the upper, solid portion of the red curve, the temperature responds to energetic disequilibrium as follows: at a given pCO_2, a perturbation in temperature upward from equilibrium is met with a cooling response and a perturbation in temperature downward is met with a warming response, until energetic equilibrium is re-established. Similarly, an increase in CO_2 from equilibrium increases albedo, which causes the planet to cool to maintain equilibrium. Thus small changes to T_{surf} or pCO_2 in this region of parameter space near the solid red curve are met with a negative feedback that tends to maintain energetic equilibrium and move the climate back to the red curve. Starting from somewhere on the red curve near the area labeled (I), if CO_2 in the atmosphere is increased by outgassing, moving rightward along the equilibrium curve, the climate will eventually reach the curve's rightmost point.

If pCO_2 is increased beyond the value at the rightmost point of the red curve, the increase in albedo is enough to push the climate system into a state of energetic disequilibrium where OLR > ASR (the light blue region in Figure 2), and the planet begins to cool. In this region, OLR responds only weakly to changes in temperature because pCO_2 is so high that the atmosphere is mostly opaque in the IR (see Figure 1b), but the albedo responds substantially, increasing as temperature decreases, since H_2O in the atmosphere falls exponentially with temperature, reducing the atmosphere's ability to absorb instellation. This produces a positive feedback with runaway cooling (stage [II] in Figure 2), where a reduction in temperature dries the atmosphere, which decreases ASR and thus pushes the system even further out of energetic equilibrium. This accelerates the cooling and reduces the ASR further. Any plausible rate of cooling vastly exceeds plausible rates of CO_2 accumulation from outgassing (compare thermal equilibration timescale of 1,000 years (Pierrehumbert, 2010) to a carbon cycle timescale of 10^6 years or more (Colbourn et al., 2015)), so the cooling trajectory is effectively straight down in T_{surf}–pCO_2 space.

After a temperature reduction of approximately 50 K, the conditions at the surface have cooled enough for CO_2 to begin to condense out onto the planetary surface, which is in this case covered by a liquid H_2O ocean. In stage (III) of the climate cycle, pCO_2 is directly dictated by surface temperature via CO_2's Clausius Clapeyron relation.

Since the climate is still in the light blue region where OLR > ASR, continued cooling drives a rapid decrease in CO_2 partial pressure, resulting in decreasing planetary albedo and increasing ASR.

Eventually, the reduction in CO_2 partial pressure increases ASR enough to re-equilibrate with the OLR at the point where arrow (III) meets arrow (IV) in Figure 2. However, this equilibrium point is unstable to further reductions in CO_2 or increases to temperature, which would shift the climate into the light red region of Figure 2, where OLR < ASR and warming is self-reinforcing due to the accumulation of atmospheric water vapor and resultant reduction in planetary albedo. As a result, any internal climate variability that acted to transiently warm the climate away from this unstable equilibrium would trigger the positive warming feedback loop represented by arrow (IV) in Figure 2, analogous to the cooling feedback loop represented by arrow (II). This warming feedback loop would finally carry the climate back to its initial energetically-stable state, at about 35.6 bar of CO_2 and $T_{surf} \approx 340$ K. From here, assuming outgassing continues, the planet would begin another iteration of this cycle of atmospheric CO_2 accumulation, runaway cooling, CO_2 rain-out, and runaway warming.

For this example of a CO_2 ocean cycle, we chose an instellation that kept the surface temperature at each pCO_2 within the range of temperatures we simulated (≤365 K). With higher S_{eff}, the maximum attainable temperature increases, and the unstable righthand branches of the S_{eff} contours shift rightward to higher pCO_2 (see Figure 1). Both of those responses to higher S_{eff} would increase the size of temperature jumps over the course of a limit cycle. Therefore, planets that start off in a limit cycling state at low S_{eff} will undergo cycles of greater and greater amplitude as their star brightens and incident instellation increases.

Up to this point, we have discussed the evolution of climates with CO_2 outgassing but without a complementary weathering feedback. This can correspond to a scenario in which weathering is "supply-limited," that is, the supply of weatherable minerals to the planetary surface is too low for weathering to keep up with the rate of CO_2 outgassing, or a scenario where liquid CO_2 or CO_2 clathrate hydrate blankets the ocean floor, suppressing weathering reactions in seafloor basalts (a scenario discussed further in Section 4). In the next subsection, we present calculations that include a simple weathering feedback.

3.3. Bistability From the Interaction of Rayleigh Scattering, Weathering, and CO_2 Condensation

With weathering included (Equation 6) and assuming an outgassing rate of 15.8×10^{12} mol yr^{-1} (2.1× an Earth-like rate of 7.5×10^{12} mol yr^{-1} drawn from Haqq-Misra et al. (2016)), our model produces a set of weathering-outgassing equilibria corresponding to the solid purple line in Figure 3. The curve has a negative slope because of the pCO_2-dependence of weathering, with lower T_{surf} required for weathering/outgassing equilibrium at higher values of pCO_2. A larger outgassing rate would result in the purple line residing at higher temperatures for a given pCO_2, changing the locations of stable and unstable equilibria, and a smaller outgassing rate would have the opposite effect. With a large enough increase in outgassing (just an increase to 2.2× the Earth-like rate, in this case), the low-CO_2 solution becomes inaccessible, and with a large enough decrease in outgassing (a reduction to below 1.0× the Earth-like rate, in this case), the high-CO_2 solution similarly disappears. Changes to the parameters in the weathering model (e.g., changing the assumed global-mean soil thickness) would have analogous effects on the locations and presence of the equilibria. With the formulation of weathering applied here (from Graham & Pierrehumbert, 2020; Maher & Chamberlain, 2014; Winnick & Maher, 2018), the behavior of the system is quite sensitive to changes in outgassing, land fraction, or weathering parameters, while the more traditional kinetically-limited formulation introduced in Walker et al. (1981) would result in less sensitivity, as demonstrated in Graham and Pierrehumbert (2020).

Figure 3 indicates the existence of two equilibrium points where outgassing (V) is balanced by weathering (W), $V = W$, and OLR = ASR for planets at a given S_{eff}, with one equilibrium climate having a higher T_{surf} and a lower pCO_2 (red and green circles *a* and *b* in Figure 3) than the other (red and green diamonds *c* and *d*). The physical reason for pairs of equilibria at each S_{eff} is CO_2's cooling effect at high partial pressures. For both S_{eff} values (0.42 and 0.47 S_{Earth}, green line and red line) plotted in Figure 3, the warmer, lower-pCO_2 climate equilibrium (*a* and *b*) is stable with respect to both its energy fluxes and its carbon fluxes, meaning a planet will return to that climate equilibrium if perturbed away from it. These stable climates are the equilibria that are typically explored in studies of silicate weathering on terrestrial planets.

Unlike its counterpart, the second equilibrium climate state where $V = W$ on each S_{eff} curve (*c* and *d*) is unstable to climatic perturbations. This is best illustrated by examining unstable equilibrium *c* with $S_{eff} = 0.42\ S_{Earth}$ in

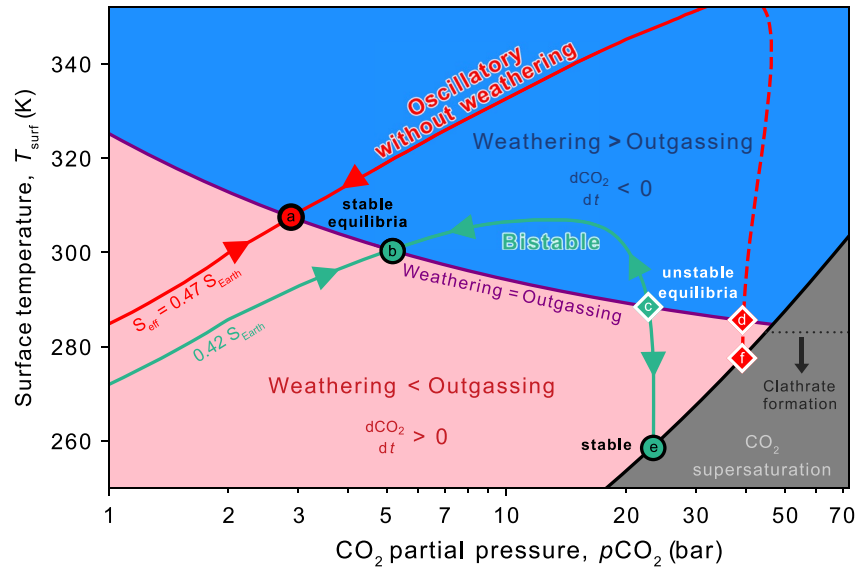

Figure 3. Comparison of stable (circles with black outline: a, b, e) and unstable (diamonds with white outline: c, d, f) climate equilibria at different instellations. The red line represents climate states with $S_{eff} = 0.47\ S_{Earth}$, with the solid part of the red line representing energetically stable climates and the dashed part of the red line representing energetically unstable climates. The green line represents climates with $S_{eff} = 0.42\ S_{Earth}$, with the possibility of bistability between an Earth-like scenario and a CO_2 condensing state. The purple line shows where weathering is equal to outgassing; the light red region below is where outgassing outpaces weathering, and the light blue region above is where weathering outpaces outgassing.

Figure 3. As noted earlier, compared to the timescale of carbon cycle response, the thermal equilibration timescale is instantaneous, so for this discussion we can assume that the climate is constrained to move along the green curve at all times. If a planet begins with a climate at point *c*, and its pCO_2 is perturbed downward (leftward on the plot), it warms up because of a reduction in CO_2 Rayleigh scattering and moves upward along the green S_{eff} isoline. This moves the planet into the blue zone of Figure 3 where $W > V$, which means that CO_2 is now being consumed by weathering faster than it can be supplied by outgassing. This imbalance in carbon fluxes leads to further reduction in pCO_2, enhancing the initial perturbation and pushing the climate deeper and deeper into the blue region. Eventually the planet reaches the peak temperature for that S_{eff}, at which point the continued reduction in CO_2 begins to cool the climate, slowing weathering until finally the planet reaches the stable equilibrium point *b*.

Conversely, if a planet begins on the unstable equilibrium *c* and pCO_2 is perturbed upward (to the right on the plot), the planet's surface will cool and the climate will move into the light red area of Figure 3, where outgassing is greater than weathering ($V > W$). With outgassing now outpacing weathering, pCO_2 will continue to grow, enhancing the initial climate perturbation until the T_{surf}–pCO_2 combination allows for CO_2 condensation at the planetary surface, at which point the carbon cycle has reached a new, stable equilibrium *e* governed by Equation 8, with the imbalance between outgassing and weathering being balanced by surface condensation of CO_2. This suggests that rocky planets at low instellation can display carbon cycle bistability, where the same geologic boundary conditions (as represented by the parameters in Equation 6) and same stellar environment can drive two very different stable equilibrium climates with pCO_2 differing by an order of magnitude, one of which displays surface CO_2 condensation and one of which does not.

The carbon cycling behavior of a planet irradiated by relative instellation of $S_{eff} = 0.47\ S_{Earth}$ (the green curve in Figure 3) is considerably different than that of the previous example because of the H_2O absorption-based radiative feedbacks that cause the CO_2 ocean limit cycling discussed in Section 3.2. In this case, even though the intersection point *f* (red-white diamond) between the $S_{eff} = 0.47\ S_{Earth}$ curve (red, dashed curve) and the CO_2 saturation vapor pressure curve (black) is stable with respect to the carbon cycle, it is unstable with respect to energy fluxes: a small perturbation in temperature upward or CO_2 downward from that point would trigger self-reinforcing warming like that exemplified by arrow (IV) in Figure 2. This would warm the planet to $T_{surf} \approx 350$ K. This is in

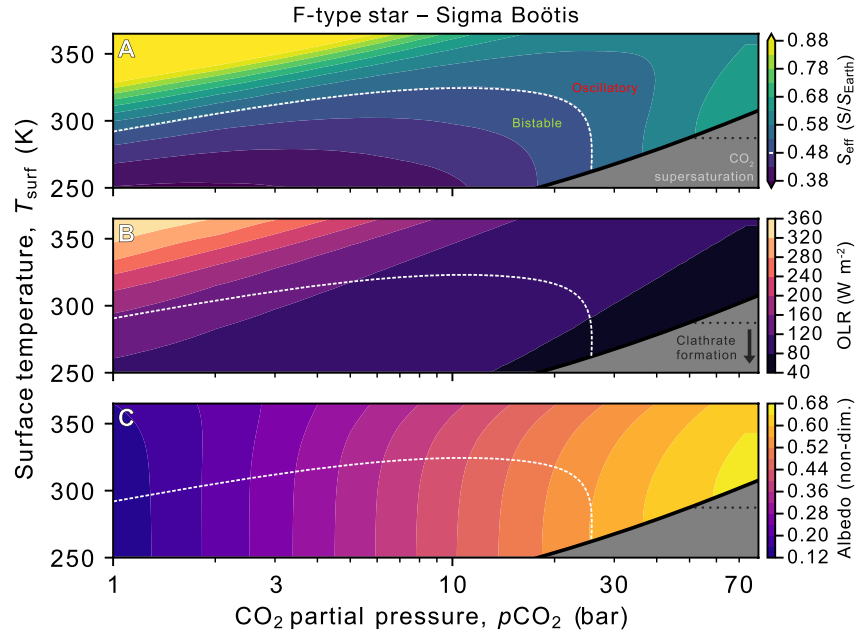

Figure 4. Energetic properties of terrestrial planetary climates irradiated by Sigma Boötis, an F2V star, at low instellation as a function of surface temperature T_{surf} (y-axes) and CO_2 partial pressure (x-axes). Panels and color coding are the same as in Figure 1.

the blue region of Figure 3, where weathering outpaces outgassing, so CO_2 would subsequently be consumed by weathering until the carbon cycle reached the stable equilibrium a, where $V = W$ for $S_{eff} = 0.47\ S_{Earth}$.

In summary, within the modeling framework applied in this article, a climate transition occurs between $S_{eff} = 0.42\ S_{Earth}$ and $S_{eff} = 0.47\ S_{Earth}$ where the climate configurations that allow for surface CO_2 condensation become energetically unstable by the same mechanism that allows for the CO_2 ocean limit cycles described in Section 3.2. However, in this case, the addition of a weathering feedback terminates the cycle before its CO_2 accumulation phase (analogous to step (I) in Figure 2) can be initiated.

3.4. Variations in Stellar Type

As noted in Section 2.1, the fiducial case studied in this article is irradiated by a solar (G2V type) spectrum drawn from Kurucz (1995). Irradiation by spectra corresponding to different stellar types can result in different climate behavior compared to what we have examined so far. Here we examine the impact of an F-type (F2V) spectrum and an M-type (M3.5V) spectrum on our basic results. In all cases, the OLR remains the same, but the planetary albedo is altered by changes to the stellar spectrum impinging on the planet. The general trend is simple to state: planets orbiting hotter, bluer stars can support the bistability between climates with and without CO_2 oceans at higher instellations than cooler, redder stars.

3.4.1. F-Type Stars

To examine the behavior of climates irradiated by F-type stars, we apply the spectrum of Sigma Boötis, an F2V star, drawn from Segura et al. (2003), in Figure 4. Because F-type stars display spectra that are shifted toward higher (bluer) frequencies than G- or M-type stars, the Rayleigh scattering effect of CO_2 is stronger for planets orbiting these stars, as Rayleigh scattering increases greatly in efficacy at shorter wavelengths. Thus, a given increase in pCO_2 leads to a larger increase in albedo for these planets, as demonstrated in Figure 4c, where the planetary albedo reaches nearly 0.68 at the highest pCO_2 shown (compared to a maximum albedo of 0.56 in simulations irradiated by a solar spectrum shown in Figure 1c). This higher sensitivity of albedo to pCO_2 leads to climate configurations where the bistability between climates with and without CO_2 oceans can persist to a higher instellation, reaching ≈54% of that of modern-day Earth (Figure 4a), compared to ≈45% for climates irradiated by the solar spectrum (Figure 1).

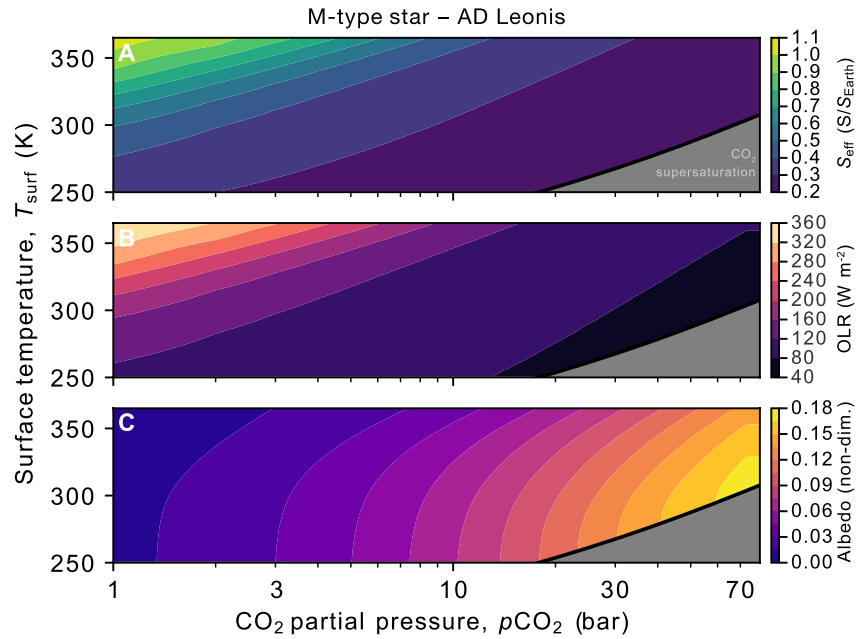

Figure 5. Energetic properties of terrestrial planetary climates irradiated by AD Leonis, an M3.5V star, at low instellation as a function of surface temperature T_{surf} (*y*-axes) and CO_2 partial pressure (*x*-axes). Panels and color coding are the same as in Figure 1.

3.4.2. M-Type Stars

To examine the behavior of planets orbiting M-type stars, we apply the spectrum of AD Leonis, an M3.5V star (Segura et al., 2005), in Figure 5. For planets orbiting M-type stars, which emit a larger proportion of their energy at lower (redder) frequencies than G- or F-type stars, the Rayleigh scattering impact of atmospheric pCO_2 is weaker. Even at the highest pCO_2 simulated in this paper (72 bar), albedo does not exceed 0.18 (Figure 5c) for planets orbiting AD Leonis, compared to maximum simulated albedo values of 0.56 and 0.68 for planets orbiting G- and F-type stars, respectively.

Interestingly, this weak dependence of planetary albedo upon CO_2 leads to a complete lack of bistable climate states in our M-star simulations. Without a substantial increase in albedo with pCO_2, CO_2's reduction of OLR dominates its radiative impact, allowing the molecule to remain a net greenhouse gas across the entirety of the parameter space we studied. Thus, for planets with functional weathering feedbacks that orbit M-type stars, we expect there to be only one stable climate state, corresponding to an Earth-like equilibrium that lacks condensed CO_2 at the surface. Correspondingly, we do not expect planets orbiting M-stars to display limit cycling between CO_2-condensing and non-condensing states, regardless of outgassing rate or TOA instellation.

4. Discussion

The interaction of liquid CO_2 and liquid H_2O at the planetary surface is fundamental to evaluating the climate state and surface geochemistry of planets with large inventories of both condensed phases. The range of temperatures over which liquid CO_2 would be stable in the presence of a liquid water ocean is relatively narrow (Marounina & Rogers, 2020). At temperatures above 304.5 K CO_2 becomes supercritical and does not condense. At temperatures below 282.91 K and pressures below 4.46 MPa (44.6 bar), mixtures of condensed CO_2, condensed H_2O, and CO_2-rich vapor are metastable, with an equilibrium state of CO_2 hydrate, a crystalline phase where water molecules encase CO_2 molecules (Wendland et al., 1999).

Experiments in Earth's ocean demonstrate that hydrate forms rapidly upon contact between liquid CO_2 and liquid H_2O, with visible masses forming over the course of just a few hours (Brewer et al., 1999). This suggests that with surface temperatures below the 282.91 K quadruple point of CO_2 hydrates mentioned in the previous paragraph, precipitation of condensed CO_2 from the atmosphere into a liquid water-rich ocean would result in immediate

formation of solid hydrates that would then sink through the water and settle on the seafloor. This may result in large-scale hydrate build-up on the ocean floor, which would suppress or halt seafloor silicate weathering, similar to high-pressure ice phases on waterworlds with extremely deep oceans (Journaux et al., 2020; Kite & Ford, 2018), removing an important CO_2 sink and making it even more difficult for a planet to exit a stable CO_2 condensing state. Other forms of low-temperature seafloor alteration would also be dramatically altered, with likely major consequences for ocean chemistry (Coogan & Gillis, 2018). Similar layered structures of hydrate and water have also been proposed for icy moons and dwarf planets (Boström et al., 2021), suggesting exploration of such bodies in the solar system may also provide insight into the structure of low-instellation terrestrial planets. Further, assuming a slow rate of subduction, the formation of large seafloor hydrate reservoirs could consume large fractions of the water in planets with Earth-like volatile inventories, since each CO_2 molecule in a hydrate is accompanied by 5.75 H_2O molecules in the most common hydrate structure (Brewer et al., 1999). Thus, under the conditions where CO_2 hydrates are stable (at temperatures below 282.91 K), a planet's subduction rate could exert a powerful direct control on ocean depth and salinity, both of which are first-order parameters in determining planetary climate and surface geochemistry (Olson et al., 2020). Finally, the coexistence of liquid CO_2 and H_2O in the air may lead to the formation of aerial CO_2 hydrates, altering the atmospheric lapse rate through latent heat release (Kasting, 1991), but it is unclear whether this would be an efficient process given the factor-of-a-thousand difference in vapor pressure between CO_2 and H_2O at relevant temperatures.

At temperatures above the hydrate quadruple point (282.9 K) and below CO_2's triple point (304.5 K), liquid CO_2 and liquid H_2O can coexist. Under pressures like those at the sea surface, liquid CO_2 is less dense than liquid H_2O, so CO_2 that rains into the ocean from the atmosphere would float and form a layer on top of the water (House et al., 2006; Marounina & Rogers, 2020). However, liquid CO_2 is also more compressible than liquid water, such that CO_2 can become denser than water at high enough pressures (House et al., 2006; Marounina & Rogers, 2020). This means that if liquid CO_2 enters the water ocean at a deep enough point, then instead of floating on top of the water, it will sink to the seafloor. Therefore, submarine CO_2 degassing in such conditions would result in the formation of a liquid CO_2 layer at the lithosphere/ocean interface. It is unclear whether silicate weathering by liquid CO_2 is possible, so the impact of this seafloor layer on carbon sequestration is an open question. All in all, the coexistence of liquid CO_2 and liquid H_2O suggests the possibility of "layer cake" oceans at the surfaces of some rocky, low-instellation planets, with an H_2O layer nestled between two CO_2 layers. This analysis remains speculative without detailed thermodynamic modeling, which is beyond the scope of this article but would make for insightful work on the surface conditions of rocky exoplanets under low instellation.

The properties of the atmosphere and ocean under CO_2 condensing conditions also have implications for the viability of origin of life scenarios on prebiotic planets akin to the Hadean Earth. In one popular school of thought regarding the origin of life, surface UV fluxes are held to be important drivers of prebiotic chemistry (Liu et al., 2021; Sasselov et al., 2020). The surface UV flux has been quantified in a variety of models approximating early Earth and early Mars atmospheres (Ranjan & Sasselov, 2016; Ranjan et al., 2017; Rugheimer et al., 2015), and atmospheres with multibar CO_2 pressures demonstrated significant UV attenuation from scattering and absorption (Ranjan et al., 2017). This suggests that atmospheres with 10 s of bar of CO_2 like those expected for the CO_2 condensing cases examined in this paper would not receive enough UV light at their surfaces to drive the relevant prebiotic chemistry. With respect to submarine origin of life scenarios, the seafloor being covered in liquid CO_2 or CO_2 hydrate in conditions with surface CO_2 condensation would preclude water-rock reactions like serpentinization (Sleep et al., 2011) or aqueous organo-metal chemistry near hot vents (Sobotta et al., 2020). It seems that several major models for the origin of life require processes that would be difficult on planets displaying the CO_2 condensing conditions explored here, even with temperate and otherwise habitable surface climates.

Given the likely reduced potential for life to emerge on CO_2 condensing planets, an observational discriminant between these worlds and their non-condensing counterparts would be useful for prioritizing targets in the search for life beyond the solar system. Here, we propose a potential method for distinguishing between CO_2 condensing and non-condensing worlds and, more generally, constraining the pCO_2 of a given exoplanet. This proposal is based on the tendency of CO_2 to dimerize and form molecular complexes at high pressures and low temperatures like those that occur in the CO_2 condensing atmospheres explored in this paper (Asfin et al., 2015; Leckenby & Robbins, 1966; Slanina et al., 1992; Tsintsarska & Huber, 2007). Similar to a method proposed for constraining O_2 partial pressure using spectroscopic O_2 dimer features in exoplanet observations (Misra et al., 2014), we suggest that high resolution spectroscopy from astronomical surveys may be able to detect CO_2 dimer features on

high-pCO_2 exoplanets. Using a quadratic fit to estimate the CO_2 dimerization equilibrium constant as a function of temperature based on data from molecular dynamics simulations (Tsintsarska & Huber, 2007), we find that CO_2 dimers would make up ≈5% of the atmosphere by molar fraction at the surface on planets with surface CO_2 condensation and surface temperatures between 273.15 K (H_2O's freezing point temperature) and 304 K (CO_2's critical temperature). Planets in the same temperature range but with lower, non-condensing pCO_2 levels have much smaller levels of dimerization; for example, an atmosphere with 6 bar of CO_2 and a surface temperature of 288 K would have a dimer fraction of less than a percent at the surface. Consequently, it may be possible to discriminate between CO_2-condensing and non-CO_2-condensing atmospheres using the presence or absence of CO_2 dimer features. These features have been detected in the near- and mid-infrared around 3,700 cm^{-1} (2.7 μm) (Jucks et al., 1987, 1988; Moazzen-Ahmadi & McKellar, 2013), 2,350 cm^{-1} (4.3 μm) (Dehghany et al., 2010; Walsh et al., 1987), and 1,250–1,400 cm^{-1} (7.1–8.0 μm) (Asfin et al., 2015; Baranov et al., 2004), placing the features within the proposed wavelength range of future telescope architectures like the Large Interferometer For Exoplanets (Dannert et al., 2022; Quanz, Absil, et al., 2021; Quanz, Ottiger, et al., 2021). Fox and Kim (1988) note the possibility of detection of CO_2 dimers in the atmospheres of Mars and Venus, where they are suggested to exist at parts-per-thousand mole fractions, much lower than the expected dimer abundance in CO_2 condensing atmospheres due to the low pressure and high temperatures on Mars and Venus respectively.

If the proposed method for constraining pCO_2 by dimer feature detection is borne out under more comprehensive examination, it may allow identification of statistical trends in pCO_2 versus instellation. Such a trend is expected if there is a population of Earth-like planets in the HZs of stars with CO_2 levels controlled by silicate weathering, which would introduce a trend of CO_2 decrease with increasing instellation (Bean et al., 2017; Checlair et al., 2019; Lehmer et al., 2020). Conversely, for the population of planets where CO_2 levels are controlled by condensation, the opposite trend would emerge: pCO_2 would increase with increasing instellation. For instance, this trend can be observed in Figure 1a, where CO_2's saturation vapor pressure curve intersects increasingly large S_{eff} contours as pCO_2 increases. Statistical comparative planetology may thus be able to distinguish populations of terrestrial exoplanets with CO_2 levels controlled by different physical and chemical processes, even if the individual measurements are too low in precision to unambiguously place a given planet into either population. A more detailed analysis of spectral response for the different climate scenarios we outline will be beneficial to analyze the optimal observational architecture (Apai et al., 2019; Quanz, Absil, et al., 2021; Quanz, Ottiger, et al., 2021; The LUVOIR Team, 2019).

4.1. Caveats

Any proposal to analyze the atmospheres of exoplanets is hindered by the potential presence of clouds, and the above is no different: high altitude cloud decks consisting of liquid or solid CO_2 or H_2O may obscure parts of the atmosphere on these CO_2 condensing planets. Clouds might also impact the OLR and albedo of these planets, potentially changing the patterns of climate behavior as a function of pCO_2 and instellation. Thus, the inclusion of clouds may alter the conclusions of this clear-sky study. In particular, if it turns out that thick, global, high-altitude cloud decks obscure the bulk of the planetary atmosphere in most high-pCO_2 climates, the bistability we identify might be muted or eliminated due to the reduced importance of CO_2 Rayleigh scattering of visible light under such conditions. Planetary albedo would instead be determined by cloud properties, with little dependence on pCO_2. We do not include clouds in our simulations for a variety of reasons. Most importantly, it is simply not possible to self-consistently calculate realistic cloud distributions in a one-dimensional model, or even to theoretically estimate cloud deck locations or cloud condensation nuclei density, so any attempt at cloud inclusion would either require arbitrary choices of all of these fundamental parameters for four distinct cloud varieties (solid H_2O, liquid H_2O, solid CO_2, liquid CO_2) or a many-dimensional parameter space sweep. Further, to our knowledge, the physical and optical properties of liquid CO_2 droplets have not been measured, making it difficult to estimate their impact without making unsupported guesses about their physical properties. The radiative impacts of CO_2 ice clouds have been examined in some detail (Forget & Pierrehumbert, 1997; Forget et al., 2013; Kitzmann, 2016, 2017), and most recent work has found that their net effect on climate is likely to be small under most parameter assumptions, though further work is warranted on this problem. The behavior of water clouds (either solid or liquid) in thick CO_2 atmospheres is relatively under-explored, though some 3D GCM studies of early Mars (Kite et al., 2021; Wordsworth et al., 2013) have examined this regime. Wordsworth et al. (2013) found a small radiative impact from water clouds in the cool, arid climates they simulated. Kite et al. (2021) found a significant climate effect from high-altitude water clouds in arid simulations and a minimal effect in simulations

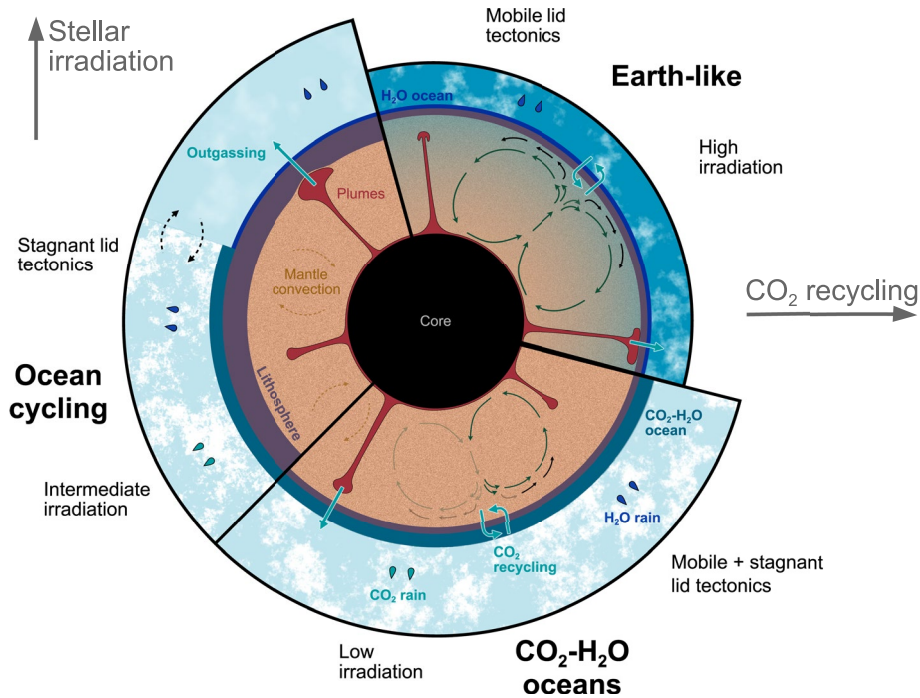

Figure 6. A schematic illustrating the climate states examined in this article. Planets with high (Earth-like) CO_2 recycling driven by efficient weathering and mobile lid tectonics that receive high stellar irradiation are likely to occupy Earth-like climate states with H_2O oceans and relatively thin atmospheres. Planets with CO_2 recycling that may range from low to high, with either mobile lid or stagnant lid tectonics, and which receive low stellar irradiation, may occupy climate states with thick CO_2 atmospheres and surface CO_2 condensation, producing oceans with both liquid CO_2 and liquid H_2O. Planets with low CO_2 recycling at intermediate instellations may oscillate between a CO_2-H_2O ocean state and a state with only H_2O oceans.

with a global ocean. Our simulations assumed an Earth-like global ocean. Thus, although clouds are a significant source of uncertainty in climate modeling, excluding their effects for a principal examination (similar to studies on the runaway greenhouse effect, e.g., Kopparapu et al., 2013) of the phenomena we are studying is justified.

We also neglected the ice-albedo feedback in our simulations because the vast majority of climates we examined had surface temperatures above freezing. Previous studies (e.g., Kadoya & Tajika, 2019; Turbet et al., 2017) have found that planets that fall into globally glaciated states at low instellation may experience surface CO_2 condensation at drastically lower pCO_2 values than the planets we have examined, since the surface temperatures of glaciated planets are tens of Kelvin colder than surface temperatures on temperate planets, though a functional seafloor weathering feedback might be enough to draw down CO_2 to low levels and prevent CO_2 condensation even in a snowball state at low instellations (e.g., Chambers, 2020). The potential for a climate transition from a snowball state with surface CO_2 condensation to a temperate state with continued surface CO_2 condensation is an interesting target for further modeling, and may provide an alternative route to a bistable CO_2-ocean-bearing climates on Earth-like planets with low instellation. In some regions of parameter space (especially low instellation and high pCO_2), the accumulation of CO_2 and resultant cooling from Rayleigh scattering could itself drive a planet into a snowball state as well, providing another intriguing and counter-intuitive climate scenario for follow-up.

Finally, we note that meridional surface temperature gradients on these planets could lead to CO_2 condensation at somewhat lower surface pressures for a given temperature than calculated here, as the poles tend to be cooler than the global mean surface temperature on planets with Earth-like obliquities and rotation rates, allowing CO_2 surface condensation with less atmospheric CO_2 accumulation. However, meridional surface temperature gradients are greatly reduced at high surface pressures (Chemke & Kaspi, 2017) and atmospheres that are made up mostly of condensable species also tend to have very small meridional temperature gradients due to the powerful winds that develop in response to the large pressure gradients that would be caused by temperature gradients in condensable-rich atmospheres. For example, the equator-to-pole temperature gradient for a pure H_2O atmosphere is calculated to be on the order of ~1 K (Ding & Pierrehumbert, 2018).

4.2. Conclusion

In summary, our simulations suggest that the interplay of the radiative properties of CO_2-rich atmospheres and the weathering of silicates leads to super-saturated and cyclic climates for planets under low irradiation for G-type and more massive stars. A qualitative sketch of the distinct climate regimes suggested by our study is shown in Figure 6. The cooling impact of Rayleigh scattering at very high CO_2 levels introduces bistability between a climate state where silicate weathering maintains CO_2 at relatively low levels and a state where CO_2 outgassing outpaces silicate weathering, maintaining CO_2 at such high levels that it condenses at the surface. At intermediate instellation, planetary temperatures can become large enough for water vapor in the atmosphere to significantly impact planetary albedo through absorption of incoming light, destabilizing surface CO_2 condensing climate states and giving rise to limit cycles between CO_2 condensing and non-condensing states. The dynamic interplay between radiation and carbon cycling profoundly impacts the climate state and surface geochemistry of otherwise Earth-like planets in the outer reaches of the liquid water HZ. These CO_2-condensing climate states are potentially distinguishable by observational characterization of CO_2 dimer features and a trend in pCO_2 versus instellation opposite to that anticipated from the nominal carbonate-silicate cycle feedback.

Data Availability Statement

We have archived the data necessary to reproduce the plots in this article at Graham et al. (2022).

Acknowledgments
RJG acknowledges scholarship funding from the Clarendon Fund and Jesus College, Oxford. TL was supported by a grant from the Simons Foundation (SCOL Award No. 611576). RTP is supported by European Research Council Advanced Grant EXOCONDENSE (Grant 740963). This AEThER publication is also funded in part by the Alfred P. Sloan Foundation under grant G202114194. We thank Robin Wordsworth, Jim Kasting, and an anonymous reviewer for helpful reviews that significantly strengthened the paper.

References

Abbot, D. S. (2016). Analytical investigation of the decrease in the size of the habitable zone due to a limited CO_2 outgassing rate. *The Astrophysical Journal*, *827*, 117. https://doi.org/10.3847/0004-637X/827/2/117

Abbot, D. S., Bloch-Johnson, J., Checlair, J., Farahat, N. X., Graham, R. J., Plotkin, D., et al. (2018). Decrease in hysteresis of planetary climate for planets with long solar days. *The Astrophysical Journal*, *854*(1), 3. https://doi.org/10.3847/1538-4357/aaa70f

Agol, E., Dorn, C., & Grimm, S. L. (2021). Refining the transit-timing and photometric analysis of TRAPPIST-1: Masses, radii, densities, dynamics, and ephemerides. *The Planetary Science Journal*, *2*, 1. https://doi.org/10.3847/PSJ/abd022

Apai, D., Milster, T. D., Kim, D. W., Bixel, A., Schneider, G., Liang, R., & Arenberg, J. (2019). A thousand earths: A very large aperture, ultralight space telescope array for atmospheric biosignature surveys. *The Astronomical Journal*, *158*(2), 83. https://doi.org/10.3847/1538-3881/ab2631

Asfin, R. E., Buldyreva, J. V., Sinyakova, T. N., Oparin, D. V., & Filippov, N. N. (2015). Communication: Evidence of stable van der Waals CO_2 clusters relevant to Venus atmosphere conditions. *The Journal of Chemical Physics*, *142*(5), 051101. https://doi.org/10.1063/1.4906874

Baranov, Y. I., Lafferty, W. J., & Fraser, G. T. (2004). Infrared spectrum of the continuum and dimer absorption in the vicinity of the O_2 vibrational fundamental in O_2/CO_2 mixtures. *Journal of Molecular Spectroscopy*, *228*(2), 432–440. https://doi.org/10.1016/j.jms.2004.04.010

Bean, J. L., Abbot, D. S., & Kempton, E. M.-R. (2017). A statistical comparative planetology approach to the hunt for habitable exoplanets and life beyond the solar system. *The Astrophysical Journal*, *841*(2), L24. https://doi.org/10.3847/2041-8213/aa738a

Berner, R. (1994). GEOCARB II; a revised model of atmospheric CO_2 over Phanerozoic time. *American Journal of Science*, *294*(1), 56–91. https://doi.org/10.2475/ajs.294.1.56

Berner, R. A., Lasaga, A. C., & Garrels, R. M. (1983). The carbonate-silicate geochemical cycle and its effect on atmospheric carbon dioxide over the past 100 million years. *American Journal of Science*, *283*(7), 641–683. https://doi.org/10.2475/ajs.283.7.641

Bonati, I., & Ramirez, R. (2021). Monthly notices of the royal astronomical society.

Boström, M., Esteso, V., Fiedler, J., Brevik, I., Buhmann, S. Y., Persson, C., et al. (2021). Self-preserving ice layers on CO_2 clathrate particles: Implications for Enceladus, Pluto, and similar ocean worlds. *Astronomy & Astrophysics*, *650*, A54. https://doi.org/10.1051/0004-6361/202040181

Brewer, P. G., Friederich, G., Peltzer, E. T., & Orr, F. M. (1999). Direct experiments on the ocean disposal of fossil fuel CO_2. *Science*, *284*(5416), 943–945. https://doi.org/10.1126/science.284.5416.943

Chambers, J. (2020). The effect of seafloor weathering on planetary habitability. *The Astrophysical Journal*, *896*(2), 96. https://doi.org/10.3847/1538-4357/ab94a4

Checlair, J. H., Abbot, D. S., Webber, R. J., Feng, Y. K., Bean, J. L., Schwieterman, E. W., et al. (2019). A statistical comparative planetology approach to maximize the scientific return of future exoplanet characterization efforts. *arXiv preprint*. arXiv:1903.05211.

Checlair, J. H., Villanueva, G. L., Hayworth, B. P. C., Olson, S. L., Komacek, T. D., Robinson, T. D., et al. (2021). Probing the capability of future direct-imaging missions to spectrally constrain the frequency of earth-like planets. *The Astronomical Journal*, *161*(3), 150. https://doi.org/10.3847/1538-3881/abdb36

Chemke, R., & Kaspi, Y. (2017). Dynamics of massive atmospheres. *The Astrophysical Journal*, *845*, 1. https://doi.org/10.3847/1538-4357/aa7742

Claire, M. W., Sheets, J., Cohen, M., Ribas, I., Meadows, V. S., & Catling, D. C. (2012). The evolution of solar flux from 0.1 nm to 160 μm: Quantitative estimates for planetary studies. *The Astrophysical Journal*, *757*(1), 95. https://doi.org/10.1088/0004-637x/757/1/95

Colbourn, G., Ridgwell, A., & Lenton, T. (2015). The time scale of the silicate weathering negative feedback on atmospheric CO_2. *Global Biogeochemical Cycles*, *29*(5), 583–596. https://doi.org/10.1002/2014gb005054

Coogan, L. A., & Gillis, K. M. (2013). Evidence that low-temperature oceanic hydrothermal systems play an important role in the silicate-carbonate weathering cycle and long-term climate regulation. *Geochemistry, Geophysics, Geosystems*, *14*(6), 1771–1786. https://doi.org/10.1002/ggge.20113

Coogan, L. A., & Gillis, K. M. (2018). Low-temperature alteration of the seafloor: Impacts on ocean chemistry. *Annual Review of Earth and Planetary Sciences*, *46*(1), 21–45. https://doi.org/10.1146/annurev-earth-082517-010027

Cox, A. N. (2015). *Allen's astrophysical quantities*. Springer.
Cronin, T. W. (2014). On the choice of average solar zenith angle. *Journal of the Atmospheric Sciences*, *71*(8), 2994–3003. https://doi.org/10.1175/jas-d-13-0392.1
Dannert, F., Ottiger, M., Quanz, S. P., Laugier, R., Fontanet, E., Gheorghe, A., et al. (2022). Large Interferometer for Exoplanets (LIFE): II. Signal simulation, signal extraction, and fundamental exoplanet parameters. *arXiv e-prints*. arXiv:2203.00471.
Dehghany, M., McKellar, A., Afshari, M., & Moazzen-Ahmadi, N. (2010). High-resolution infrared spectroscopy of carbon dioxide dimers, trimers, and larger clusters. *Molecular Physics*, *108*(17), 2195–2205. https://doi.org/10.1080/00268976.2010.496742
Ding, F., & Pierrehumbert, R. T. (2018). Global or local pure condensible atmospheres: Importance of horizontal latent heat transport. *The Astrophysical Journal*, *867*(1), 54. https://doi.org/10.3847/1538-4357/aae38c
Edwards, J., & Slingo, A. (1996). Studies with a flexible new radiation code. I: Choosing a configuration for a large-scale model. *Quarterly Journal of the Royal Meteorological Society*, *122*(531), 689–719. https://doi.org/10.1002/qj.49712253107
Fischer, R. A., Cottrell, E., Hauri, E., Lee, K. K. M., & Le Voyer, M. (2020). The carbon content of Earth and its core. *Proc. Nat. Acad. Sci. USA*, *117*(16), 8743–8749. https://doi.org/10.1073/pnas.1919930117
Foley, B. J. (2015). The role of plate tectonic–climate coupling and exposed land area in the development of habitable climates on rocky planets. *The Astrophysical Journal*, *812*(1), 36. https://doi.org/10.1088/0004-637x/812/1/36
Forget, F., & Pierrehumbert, R. T. (1997). Warming early Mars with carbon dioxide clouds that scatter infrared radiation. *Science*, *278*(5341), 1273–1276. https://doi.org/10.1126/science.278.5341.1273
Forget, F., Wordsworth, R., Millour, E., Madeleine, J. B., Kerber, L., Leconte, J., et al. (2013). 3D modelling of the early martian climate under a denser CO_2 atmosphere: Temperatures and CO_2 ice clouds. *Icarus*, *222*(1), 81–99. https://doi.org/10.1016/j.icarus.2012.10.019
Fox, K., & Kim, S. J. (1988). Spectra of van der Waals complexes (dimers) with applications to planetary atmospheres. *Journal of Quantitative Spectroscopy and Radiative Transfer*, *40*(3), 177–184. https://doi.org/10.1016/0022-4073(88)90111-2
Gaudi, B. S., Seager, S., Mennesson, B., Kiessling, A., Warfield, K., Cahoy, K., et al. (2020). The Habitable Exoplanet Observatory (HabEx) mission concept study final report. *arXiv e-prints*. arXiv:2001.06683.
Gerlach, T. (2011). Volcanic versus anthropogenic carbon dioxide. *Eos, Transactions American Geophysical Union*, *92*(24), 201–202. https://doi.org/10.1029/2011eo240001
Gordon, I. E., Rothman, L. S., Hill, C., Kochanov, R. V., Tan, Y., Bernath, P. F., et al. (2017). The HITRAN2016 molecular spectroscopic database. *Journal of Quantitative Spectroscopy & Radiative Transfer*, *203*, 3. https://doi.org/10.1016/j.jqsrt.2017.06.038
Graham, R., Lichtenber, T., & Pierrehumbert, R. (2022). Data for "CO_2 ocean bistability on terrestrial exoplanets". *Zenodo*. https://doi.org/10.5281/zenodo.6546737
Graham, R., Lichtenberg, T., Boukrouche, R., & Pierrehumbert, R. (2021). A multispecies pseudoadiabat for simulating condensable-rich exoplanet atmospheres. *Planetary Science Journal*, *2*, 207. https://doi.org/10.3847/PSJ/ac214c
Graham, R., & Pierrehumbert, R. (2020). Thermodynamic and energetic limits on continental silicate weathering strongly impact the climate and habitability of wet, rocky worlds. *The Astrophysical Journal*, *896*(2), 115. https://doi.org/10.3847/1538-4357/ab9362
Grewal, D. S., Dasgupta, R., & Farnell, A. (2020). The speciation of carbon, nitrogen, and water in magma oceans and its effect on volatile partitioning between major reservoirs of the Solar System rocky bodies. *Geochimica et Cosmochimica Acta*, *280*, 281–301. https://doi.org/10.1016/j.gca.2020.04.023
Gruszka, M., & Borysow, A. (1997). Roto-translational collision-induced absorption of CO_2 for the atmosphere of venus at frequencies from 0 to 250 cm^{-1}, at temperatures from 200 to 800 K. *Icarus*, *129*(1), 172–177. https://doi.org/10.1006/icar.1997.5773
Hakim, K., Bower, D. J., Tian, M., Deitrick, R., Auclair-Desrotour, P., Kitzmann, D., et al. (2021). Lithologic controls on silicate weathering regimes of temperate planets. *The Planetary Science Journal*, *2*, 49. https://doi.org/10.3847/psj/abe1b8
Halevy, I., Pierrehumbert, R. T., & Schrag, D. P. (2009). Radiative transfer in CO_2-rich paleoatmospheres. *Journal of Geophysical Research*, *114*(D18), D18112. https://doi.org/10.1029/2009jd011915
Haqq-Misra, J., Kopparapu, R. K., Batalha, N. E., Harman, C. E., & Kasting, J. F. (2016). *The Astrophysical Journal*, *827*(2), 120. https://doi.org/10.3847/0004-637x/827/2/120
Hayworth, B. P., & Foley, B. J. (2020). Waterworlds may have better climate buffering capacities than their continental counterparts. *The Astrophysical Journal Letters*, *902*(1), L10. https://doi.org/10.3847/2041-8213/abb882
Hirschmann, M. M., Bergin, E. A., Blake, G. A., Ciesla, F., & Li, J. (2021). Early volatile depletion on planetesimals inferred from C–S systematics of iron meteorite parent bodies. *Proceedings of the National Academy of Sciences*, *118*(13), e2026779118. https://doi.org/10.1073/pnas.2026779118
House, K. Z., Schrag, D. P., Harvey, C. F., & Lackner, K. S. (2006). Permanent carbon dioxide storage in deep-sea sediments. *Proceedings of the National Academy of Sciences*, *103*(33), 12291–12295. https://doi.org/10.1073/pnas.0605318103
Journaux, B., Kalousová, K., Sotin, C., Tobie, G., Vance, S., Saur, J., et al. (2020). Large ocean worlds with high-pressure ices. *Space Science Reviews*, *216*(1), 7. https://doi.org/10.1007/s11214-019-0633-7
Jucks, K., Huang, Z., Dayton, D., Miller, R., & Lafferty, W. (1987). The structure of the carbon dioxide dimer from near infrared spectroscopy. *The Journal of Chemical Physics*, *86*(8), 4341–4346. https://doi.org/10.1063/1.451895
Jucks, K., Huang, Z., & Miller, R. (1988). Infrared spectroscopy of the hydrogen cyanide dimer. *The Journal of Chemical Physics*, *88*(10), 2185–6067. https://doi.org/10.1063/1.454498
Kadoya, S., & Tajika, E. (2019). Outer limits of the habitable zones in terms of climate mode and climate evolution of earth-like planets. *The Astrophysical Journal*, *875*(1), 7. https://doi.org/10.3847/1538-4357/ab0aef
Karman, T., Miliordos, E., Hunt, K. L. C., Groenenboom, G. C., & van der Avoird, A. (2015). Quantum mechanical calculation of the collision-induced absorption spectra of N_2–N_2 with anisotropic interactions. *Journal of Chemical Physics*, *142*(8), 084306. https://doi.org/10.1063/1.4907917
Kasting, J. F. (1991). CO_2 condensation and the climate of early Mars. *Icarus*, *94*, 1–13. https://doi.org/10.1016/0019-1035(91)90137-i
Kasting, J. F., Whitmire, D. P., & Reynolds, R. T. (1993). Habitable zones around main sequence stars. *Icarus*, *101*(1), 108–128. https://doi.org/10.1006/icar.1993.1010
Kite, E., Manga, M., & Gaidos, E. (2009). Geodynamics and rate of volcanism on massive Earth-like planets. *The Astrophysical Journal*, *700*(2), 1732–1749. https://doi.org/10.1088/0004-637X/700/2/1732
Kite, E. S., & Ford, E. B. (2018). Habitability of exoplanet waterworlds. *The Astrophysical Journal*, *864*(1), 75. https://doi.org/10.3847/1538-4357/aad6e0
Kite, E. S., Steele, L. J., Mischna, M. A., & Richardson, M. I. (2021). Warm early Mars surface enabled by high-altitude water ice clouds. *Proceedings of the National Academy of Sciences*, *118*(18), e2101959118. https://doi.org/10.1073/pnas.2101959118

Kitzmann, D. (2016). Revisiting the scattering greenhouse effect of CO_2 ice clouds. *The Astrophysical Journal Letters*, *817*(2), L18. https://doi.org/10.3847/2041-8205/817/2/l18

Kitzmann, D. (2017). Clouds in the atmospheres of extrasolar planets. *Astronomy & Astrophysics*, *600*, A111. https://doi.org/10.1051/0004-6361/201630029

Kopparapu, R. K., Ramirez, R., Kasting, J. F., Eymet, V., Robinson, T. D., Mahadevan, S., et al. (2013). Habitable zones around main-sequence stars: New estimates. *The Astrophysical Journal*, *765*(2), 131. https://doi.org/10.1088/0004-637x/765/2/131

Korenaga, J. (2010). On the likelihood of plate tectonics on super-earths: Does size matter? *The Astrophysical Journal Letters*, *725*(1), L43–L46. https://doi.org/10.1088/2041-8205/725/1/l43

Krijt, S., Bosman, A. D., Zhang, K., Schwarz, K. R., Ciesla, F. J., & Bergin, E. A. (2020). CO depletion in protoplanetary disks: A unified picture combining physical sequestration and chemical processing. *Acta Pathologica Japonica*, *899*(2), 134. https://doi.org/10.3847/1538-4357/aba75d

Kump, L. R., Brantley, S. L., & Arthur, M. A. (2000). Chemical weathering, atmospheric CO_2, and climate. *Annual Review of Earth and Planetary Sciences*, *28*(1), 611–667. https://doi.org/10.1146/annurev.earth.28.1.611

Kurucz, R. L. (1995). *CD-ROM 23*. Smithsonian Astrophysical Observatory.

Leckenby, R., & Robbins, E. (1966). The observation of double molecules in gases. *Proceedings of the Royal Society of London. Series A. Mathematical and Physical Sciences*, *291*, 389. https://doi.org/10.1098/rspa.1966.0102

Lehmer, O. R., Catling, D. C., & Krissansen-Totton, J. (2020). Carbonate-silicate cycle predictions of Earth-like planetary climates and testing the habitable zone concept. *Nature Communications*, *11*, 1. https://doi.org/10.1038/s41467-020-19896-2

Lenardic, A. (2018). The diversity of tectonic modes and thoughts about transitions between them. *Philosophical Transactions of the Royal Society A: Mathematical, Physical & Engineering Sciences*, *376*(2132), 20170416. https://doi.org/10.1098/rsta.2017.0416

Li, J., Bergin, E. A., Blake, G. A., Ciesla, F. J., & Hirschmann, M. M. (2021). Earth's carbon deficit caused by early loss through irreversible sublimation. *Science Advances*, *7*(14), eabd3632. https://doi.org/10.1126/sciadv.abd3632

Li, J., Scinocca, J., Lazare, M., McFarlane, N., von Salzen, K., & Solheim, L. (2006). Ocean surface albedo and its impact on radiation balance in climate models. *Journal of Climate*, *19*(24), 6314–6333. https://doi.org/10.1175/jcli3973.1

Lichtenberg, T., Bower, D. J., Hammond, M., Boukrouche, R., Sanan, P., Tsai, S., & Pierrehumbert, R. T. (2021). Vertically resolved magma ocean–protoatmosphere evolution: H_2, H_2O, CO_2, CH_4, CO, O_2, and N_2 as primary absorbers. *Journal of Geophysical Research: Planets*, *126*(2), e2020JE006711. https://doi.org/10.1029/2020je006711

Lichtenberg, T., & Krijt, S. (2021). System-level fractionation of carbon from disk and planetesimal processing. *Acta Pathologica Japonica*, *913*(2), L20. https://doi.org/10.3847/2041-8213/abfdce

Lichtenberg, T., Schaefer, L. K., Nakajima, M., & Fischer, R. A. (2022). Geophysical evolution during rocky planet formation. *arXiv e-prints*. arXiv:2203.10023.

Liu, Z., Wu, L.-F., Kufner, C. L., Sasselov, D. D., Fischer, W. W., & Sutherland, J. D. (2021). Prebiotic photoredox synthesis from carbon dioxide and sulfite. *Nature Chemistry*, *13*(11), 1126–1132. https://doi.org/10.1038/s41557-021-00789-w

Maher, K., & Chamberlain, C. (2014). Hydrologic regulation of chemical weathering and the geologic carbon cycle. *Science*, *343*(6178), 1502–1504. https://doi.org/10.1126/science.1250770

Marounina, N., & Rogers, L. A. (2020). Internal structure and CO_2 reservoirs of habitable water worlds. *The Astrophysical Journal*, *890*(2), 107. https://doi.org/10.3847/1538-4357/ab68e4

Marshall, B. R., & Smith, R. C. (1990). Raman scattering and in-water ocean optical properties. *Applied Optics*, *29*(1), 71. https://doi.org/10.1364/ao.29.000071

Menou, K. (2015). Climate stability of habitable Earth-like planets. *Earth and Planetary Science Letters*, *429*, 20–24. https://doi.org/10.1016/j.epsl.2015.07.046

Misra, A., Meadows, V., Claire, M., & Crisp, D. (2014). Using dimers to measure biosignatures and atmospheric pressure for terrestrial exoplanets. *Astrobiology*, *14*(2), 67–86. https://doi.org/10.1089/ast.2013.0990

Mlawer, E. J., Payne, V. H., Moncet, J. L., Delamere, J. S., Alvarado, M. J., & Tobin, D. C. (2012). Development and recent evaluation of the MT_CKD model of continuum absorption. *Philos. Trans. Royal Soc. A*, *370*(1968), 2520–2556. https://doi.org/10.1098/rsta.2011.0295

Moazzen-Ahmadi, N., & McKellar, A. (2013). Spectroscopy of dimers, trimers and larger clusters of linear molecules. *International Reviews in Physical Chemistry*, *32*(4), 611–650. https://doi.org/10.1080/0144235x.2013.813799

Öberg, K. I., & Bergin, E. A. (2021). Astrochemistry and compositions of planetary systems. *Physics Reports*, *893*, 1–48. https://doi.org/10.1016/j.physrep.2020.09.004

Oki, T., Agata, Y., Kanae, S., Saruhashi, T., Yang, D., & Musiake, K. (2001). Global assessment of current water resources using total runoff integrating pathways. *Hydrological Sciences Journal*, *46*(6), 983–995. https://doi.org/10.1080/02626660109492890

Olson, S. L., Jansen, M., & Abbot, D. S. (2020). Oceanographic considerations for exoplanet life detection. *The Astrophysical Journal*, *895*(1), 19. https://doi.org/10.3847/1538-4357/ab88c9

Paradise, A., & Menou, K. (2017). GCM simulations of unstable climates in the habitable zone. *The Astrophysical Journal*, *848*, 1. https://doi.org/10.3847/1538-4357/aa8b1c

Penman, D. E., Rugenstein, J. K. C., Ibarra, D. E., & Winnick, M. J. (2020). Silicate weathering as a feedback and forcing in Earth's climate and carbon cycle. *Earth-Science Reviews*, *209*, 103298. https://doi.org/10.1016/j.earscirev.2020.103298

Pierrehumbert, R. T. (2010). *Principles of planetary climate*. Cambridge University Press.

Pluriel, W., Marcq, E., & Turbet, M. (2019). Modeling the albedo of Earth-like magma ocean planets with H_2O-CO_2 atmospheres. *Icarus*, *317*, 583–590. https://doi.org/10.1016/j.icarus.2018.08.023

Quanz, S. P., Absil, O., Benz, W., Bonfils, X., Berger, J. P., Defrere, D., et al. (2021). Atmospheric characterization of terrestrial exoplanets in the mid-infrared: Biosignatures, habitability, and diversity. *Experimental Astronomy*, *1*. https://doi.org/10.1007/s10686-021-09791-z

Quanz, S. P., Ottiger, M., Fontanet, E., Kammerer, J., Menti, F., Dannert, F., et al. (2021). Large Interferometer For Exoplanets (LIFE): I. Improved exoplanet detection yield estimates for a large mid-infrared space-interferometer mission. *arXiv e-prints*. arXiv:2101.07500.

Ramirez, R. M., & Levi, A. (2018). The ice cap zone: A unique habitable zone for ocean worlds. *Monthly Notices of the Royal Astronomical Society*, *477*, 4627. https://doi.org/10.1093/mnras/sty761

Ranjan, S., & Sasselov, D. D. (2016). Influence of the UV environment on the synthesis of prebiotic molecules. *Astrobiology*, *16*(1), 68–88. https://doi.org/10.1089/ast.2015.1359

Ranjan, S., Wordsworth, R., & Sasselov, D. D. (2017). Atmospheric constraints on the surface UV environment of Mars at 3.9 Ga relevant to prebiotic chemistry. *Astrobiology*, *17*(8), 687–708. https://doi.org/10.1089/ast.2016.1596

Rimstidt, J. D., Brantley, S. L., & Olsen, A. A. (2012). Systematic review of forsterite dissolution rate data. *Geochimica et Cosmochimica Acta*, *99*, 159–178. https://doi.org/10.1016/j.gca.2012.09.019

Rugheimer, S., Segura, A., Kaltenegger, L., & Sasselov, D. (2015). UV surface environment of Earth-like planets orbiting FGKM stars through geological evolution. *The Astrophysical Journal*, *806*(1), 137. https://doi.org/10.1088/0004-637x/806/1/137

Sasselov, D. D., Grotzinger, J. P., & Sutherland, J. D. (2020). The origin of life as a planetary phenomenon. *Science Advances*, *6*, eaax3419. https://doi.org/10.1126/sciadv.aax3419

Schneider, T., Kaul, C. M., & Pressel, K. G. (2019). Possible climate transitions from breakup of stratocumulus decks under greenhouse warming. *Nature Geoscience*, *12*(3), 163–167. https://doi.org/10.1038/s41561-019-0310-1

Segura, A., Kasting, J., Meadows, V., Cohen, M., Scalo, J., Crisp, D., et al. (2005). Biosignatures from Earth-like planets around M dwarfs. *Astrobiology*, *5*(6), 706–725. https://doi.org/10.1089/ast.2005.5.706

Segura, A., Krelove, K., Kastings, J. F., Sommerlatt, D., Meadows, V., Crisp, D., et al. (2003). Ozone concentrations and ultraviolet fluxes on Earth-like planets around other stars. *Astrobiology*, *3*(4), 689–708. https://doi.org/10.1089/153110703322736024

Slanina, Z., Fox, K., & Kim, S. J. (1992). A computational evaluation of altitude profiles of the equilibrium monomeric-dimeric CO_2 fractions in the atmosphere of Venus. *Thermochimica Acta*, *200*, 33–39. https://doi.org/10.1016/0040-6031(92)85103-3

Sleep, N. H., Bird, D. K., & Pope, E. C. (2011). Serpentinite and the dawn of life. *Philosophical Transactions of the Royal Society B: Biological Sciences*, *366*(1580), 2857–2869. https://doi.org/10.1098/rstb.2011.0129

Sobotta, J., Geisberger, T., Moosmann, C., Scheidler, C. M., Eisenreich, W., Wachtershauser, G., & Huber, C. (2020). A possible primordial acetyleno/carboxydotrophic core metabolism. *Life*, *10*(4), 35. https://doi.org/10.3390/life10040035

Soto, A., Mischna, M., Schneider, T., Lee, C., & Richardson, M. (2015). Martian atmospheric collapse: Idealized GCM studies. *Icarus*, *250*, 553–569. https://doi.org/10.1016/j.icarus.2014.11.028

The LUVOIR Team. (2019). The LUVOIR mission concept study final report. *arXiv e-prints*. arXiv:1912.06219.

Tsintsarska, S., & Huber, H. (2007). The equilibrium constant of carbon dioxide dimerization and the lifetime of the dimer. *Molecular Physics*, *105*(1), 25–31. https://doi.org/10.1080/00268970601126726

Turbet, M., Forget, F., Leconte, J., Charnay, B., & Tobie, G. (2017). CO_2 condensation is a serious limit to the deglaciation of Earth-like planets. *Earth and Planetary Science Letters*, *11*, 11–21. https://doi.org/10.1016/j.epsl.2017.07.050

Valencia, D., O'Connell, R., & Sasselov, D. D. (2007). Inevitability of plate tectonics on super-earths. *The Astrophysical Journal*, *670*(1), L45–L48. https://doi.org/10.1086/524012

Vardavas, I., & Carver, J. H. (1984). Solar and terrestrial parameterizations for radiative-convective models. *Planetary and Space Science*, *32*(10), 1307–1325. https://doi.org/10.1016/0032-0633(84)90074-6

Venturini, J., Guilera, O. M., Haldemann, J., Ronco, M. P., & Mordasini, C. (2020). The nature of the radius valley. *Astronomy and Astrophysics*, *643*, L1. https://doi.org/10.1051/0004-6361/202039141

von Paris, P., Grenfell, J. L., Hedelt, P., Rauer, H., Selsis, F., & Stracke, B. (2013). Atmospheric constraints for the CO_2 partial pressure on terrestrial planets near the outer edge of the habitable zone. *Astronomy & Astrophysics*, *549*, A94. https://doi.org/10.1051/0004-6361/201219684

Walker, J. C. G., Hays, P. B., & Kasting, J. F. (1981). A negative feedback mechanism for the long-term stabilization of Earth's surface temperature. *Journal of Geophysical Research*, *86*(C10), 9776. https://doi.org/10.1029/jc086ic10p09776

Walsh, M., England, T., Dyke, T., & Howard, B. (1987). Pulsed molecular beam infrared absorption spectroscopy of CO_2 dimer. *Chemical Physics Letters*, *142*(3–4), 265–270. https://doi.org/10.1016/0009-2614(87)80935-1

Wendland, M., Hasse, H., & Maurer, G. (1999). Experimental pressure−temperature data on three- and four-phase equilibria of fluid, hydrate, and ice phases in the system carbon dioxide−water. *Journal of Chemical & Engineering Data*, *44*(5), 901–906. https://doi.org/10.1021/je980208o

West, A. J., Galy, A., & Bickle, M. (2005). Tectonic and climatic controls on silicate weathering. *Earth and Planetary Science Letters*, *235*(1–2), 211–228. https://doi.org/10.1016/j.epsl.2005.03.020

Winnick, M. J., & Maher, K. (2018). Relationships between CO_2, thermodynamic limits on silicate weathering, and the strength of the silicate weathering feedback. *Earth and Planetary Science Letters*, *485*, 111–120. https://doi.org/10.1016/j.epsl.2018.01.005

Wordsworth, R., Forget, F., & Eymet, V. (2010). Infrared collision-induced and far-line absorption in dense CO_2 atmospheres. *Icarus*, *210*(2), 992–997. https://doi.org/10.1016/j.icarus.2010.06.010

Wordsworth, R., Forget, F., Millour, E., Head, J., Madeleine, J. B., & Charnay, B. (2013). Global modelling of the early martian climate under a denser CO_2 atmosphere: Water cycle and ice evolution. *Icarus*, *222*, 1–19. https://doi.org/10.1016/j.icarus.2012.09.036

Wordsworth, R., Forget, F., Selsis, F., Madeleine, J. B., Millour, E., & Eymet, V. (2010). Is Gliese 581d habitable? Some constraints from radiative-convective climate modeling. *Astronomy & Astrophysics*, *522*, A22. https://doi.org/10.1051/0004-6361/201015053

Wordsworth, R. D., & Pierrehumbert, R. T. (2013). Water loss from terrestrial planets with CO_2-rich atmospheres. *The Astrophysical Journal*, *778*(2), 154. https://doi.org/10.1088/0004-637x/778/2/154

Zeng, L., Jacobsen, S. B., Sasselov, D. D., Petaev, M. I., Vanderburg, A., Lopez-Morales, M., et al. (2019). Growth model interpretation of planet size distribution. *Proceedings of the National Academy of Sciences*, *116*(20), 9723–9728. https://doi.org/10.1073/pnas.1812905116